Supporting Information

TABLE OF CONTENTS

EXPERIMENTAL SECTION

Pdot Preparation and Characterization

Poly[(9,9-dihexyl-2,7-(2-cyanodivinylene)-fluorenylenyl-2,7-diyl)] (CN-PDHFV, MW 25,000), poly[(9,9-dioctyl-2,7-divinylenefluorenylene)-alt-co-{2-methoxy5-(2-ethylhexyloxy)-1,4-phenylene}] (PFPV, MW 30,000), poly[(9,9-dioctylfluorenyl-2,7-diyl)-*co*-(1,4-benzo-{2,1′,3}-thiadiazole)] (F8BT, MW 13,500), poly[2-methoxy-5-(2-ethylhexyloxy)-1,4-(1-cyanovinylene-1,4-phenylene)] (CN-PPV, MW 13,000) were purchased from ADS Dyes, Inc. Poly[(N,N′-bis(2-octyldodecyl)naphthalene-1,4,5,8-bis(dicarboximide)-2,6-diyl)-alt-5,5′-(3,3′-difluoro-2,2′-bithiophene)] (PNDI-2F) was purchased from Ossila, Ltd. Poly[(N,N′-bis(2-octyldodecyl)naphthalene-1,4,5,8-bis(dicarboximide)-2,6-diyl)-alt-5,5′-(2,2′-bithiophene)] (PNDI-2T), poly(styrene-co-maleic anhydride) (PSMA, MW 1,900), tetrahydrofuran (THF, HPLC grade, 99.9%), beta-mercaptoethanol (BME) and (3-Aminopropyl) trimethoxysilane (APTMS) were purchased from Sigma-Aldrich. All chemicals were used as received without further purification. Semiconducting polymer dots (Pdots) were prepared using a previously reported nanoprecipitation method.[1] CN-PDHFV, PFPV, F8BT, CN-PPV and PSMA were dissolved in THF and diluted to 20 ppm. Electron-accepting polymers PNDI-2T and PNDI-2F were dissolved in THF and diluted to 10 ppm. The semiconducting polymers and electron acceptors were mixed at various ratios to create precursor solutions of varying dopant percentages (10%, 20%, and 40% w/w). After thorough mixing, PSMA solution was added to the mixture to make the final precursor containing 10% PSMA (w/w). 2 mL of the precursor solution was rapidly injected into 8 mL of water under mild sonication. The mixed solution was then heated under nitrogen atmosphere to remove THF solvent. After THF evaporation, the sample was filtered through a 100 nm polyvinylidene fluoride (PVDF) membrane (Millipore) to remove aggregates. The nanoparticle size distribution was determined by dynamic light scattering (DLS) and transmission electron microscopy (TEM). DLS measurements were conducted using a Zetasizer (Malvern Panalytical, UK) at 25°C with a scattering angle of 173° and an acquisition time of 180 s. PS nanospheres (Thermo Fisher, 24 nm) were used as a size standard. NNLS fitting was employed to determine particle size distributions. To prepare TEM samples, Pdots suspensions were drop-cast onto a carbon-coated copper grid. After drying, the Pdots were imaged using an FEI Tecnai F20 TEM. UV-vis absorbance and fluorescence spectra were collected using a Beckman Coulter DU720 spectrophotometer and a Perkin Elmer LS55 fluorometer, respectively.

Bioconjugation and Cell Labeling

Streptavidin (SA), 1-ethyl-3-(3-dimethylaminopropyl)carbodiimide (EDC), poly(ethylene glycol) (PEG, MW 3,350), bovine serum albumin (BSA), triton X-100, 1,4-piperazinediethanesulfonic acid (PIPES), ethyleneglycol-bis(β-aminoethyl)-N,N,N′,N′-tetraacetic acid (EGTA), $NaBH_4$, and $MgCl_2$ were purchased from Sigma-Aldrich. Glutaraldehyde (GA) and paraformaldehyde (PFA) were purchased from Electron Microscopy Sciences. Rabbit monoclonal biotinylated anti-alpha

tubulin antibody (clone RM113, MA5-27888) was purchased from Thermo Fisher. Mouse monoclonal anti-clathrin heavy chain antibody (clone X22, ab2731) was purchased from Abcam. Goat anti-mouse secondary antibody was purchased from BioLegend (405301). Freshly prepared Pdots were conjugated to SA or secondary antibody via an EDC-catalyzed reaction as described previously.[2] 1 mL of Pdots suspension (~50 μg/mL) was mixed with 20 μL of PEG (5% wt), 20 μL of N-2-hydroxyethylpiperazine-N-2-ethane sulfonic acid buffer (HEPES, 1 M, pH 7.4), 60 μL of SA or secondary antibody (1 mg/mL), and 20 μL of EDC (5 mg/mL). After 4 h of reaction, the solution was centrifuged (Amicon Ultra-4, MWCO 100,000 for SA conjugation; Sartorius Vivaspin 500, MWCO 300,000 for secondary antibody conjugation) and re-diluted 3 times in HEPES buffer containing 0.2% BSA (w/v). The final solution was concentrated to 0.5 mL and loaded into a size-exclusion column packed with Sephacryl S-400 HR resin; 20 mM HEPES with 0.1% PEG was used as buffer. The purified Pdots were collected from the colored band eluate from the column. 24 h prior to fixation, BS-C-1 cells (African green monkey kidney, ATCC #CCL-26) were seeded in 8-well chambered slides (Ibidi, 80821) and cultured with Eagle's minimum essential medium (EMEM, ATCC, 30-2003). The extraction, fixation, block/perm buffers were prepared as described previously.[3] The extraction buffer contained 100 mM PIPES, 1 mM EGTA, 1 mM $MgCl_2$, and 0.5% (v/v) Triton X-100. The fixation buffer contained 100 mM PIPES, 1 mM EGTA, 1 mM $MgCl_2$, 3.2% PFA, and 0.1% GA (no GA was added when labeling clathrin-coated pits). The block/perm buffer was prepared by adding 3% BSA (w/v) and 0.5% Triton (v/v) X-100 to phosphate buffered saline (1×PBS pH 7.4). Before labeling, BS-C-1 cells were extracted for 30 s, fixed for 10 min, reduced in freshly prepared $NaBH_4$ for 10 min (the reduction procedure was skipped when labeling CCPs), then permeabilized for 45 min using the buffers described above. The sample was rinsed with PBS 3 times after the fixation, reduction, and permeabilization steps. To label microtubules with SA-conjugated Pdots, the permeabilized cells were first incubated with 200 μL of biotinylated rabbit anti-tubulin antibody (10 μg/mL) for 1 h at 25°C, then washed 3 times with PBS and incubated with 200 μL of SA-conjugated Pdots (50 μg/mL) for 1 h at 25°C. To label CCPs, the permeabilized cells were first incubated with 200 μL of mouse anti-clathrin antibody (4 μg/mL) for 1 h at 25°C, then washed 3 times with PBS and incubated with 200 μL of the secondary antibody-conjugated Pdots (50 μg/mL) for 1 h at 25°C. All antibodies and Pdots were diluted in block/perm buffer. After incubation, the sample was washed 3 times with PBS and stored at 4°C. In a two-color experiment involving labeling both MTs and CCPs, the procedures described above were followed sequentially with the sample rinsed thoroughly with PBS in between.

Single-Particle Imaging

Single-particle imaging was performed using a custom wide-field microscope (Nikon, TE2000-U). The excitation sources included a 405 nm continuous wave (CW) laser (Coherent, Obis, 50 mW), a 455 diode laser (Osram, 80 mW), a 488 nm CW laser (Coherent, Sapphire, 100 mW), a 532 nm CW diode laser (Roithner, 50 mW) and a 640 nm CW laser (Coherent, Obis, 100 mW). A 500 long-pass (Chroma, 500 DCLP) or a multi-band dichroic (Chroma,

ZT405/488/532/640rpc-XT) was used to reflect excitation light to a high numerical aperture objective (Nikon, Plan Apo TIRF, 100×, 1.45 NA, oil). The full-width half-maxima (FWHM) of the laser profiles were ~30–40 μm at the sample plane. The emission filters used for 10% PNDI-2F-doped CN-PDHFV Pdots, 10% PNDI-2T-doped PFPV Pdots, 20% PNDI-2F-doped F8BT Pdots, and 10% PNDI-2F-doped CN-PPV Pdots were 535/70 nm (Chroma, ET535/70m), 609/181 nm (Semrock, FF01-609/181-25), 609/181 nm (Semrock, FF01-609/181-25), and 650/150 nm (Semrock, FF01-650/150-25), respectively. The filtered emission light passed through a cylindrical lens (Thorlabs, LJ1516RM-A) and a pair of identical achromatic lenses (Thorlabs, AC254-050-A) before focusing onto a sCMOS camera (Hamamatsu, Orca flash 4.0). The detector settings were 16 bits per pixel, 0.5 gain, rolling shutter mode. From analysis of shot noise from a blank coverslip, the experimental gain factor was determined to be 0.51 electrons per count. The pixel pitch was determined from imaging a TEM calibration grid, which yielded 110 nm/pixel. To prepare imaging samples, diluted Pdot suspension was drop-cast onto coverslips functionalized with APTMS. The Pdots were imaged in oxygen scavenging glucose oxidase (GLOX) buffer, for 1200 s using a frame rate of 50 or 100 Hz. A motorized stage (ASI, MS-2000) was used to position the sample. A commercial autofocus system (ASI, CRIFF) was used to keep the system in focus during imaging. For single particle imaging, the power of the excitation laser was adjusted to yield a power density of 2 kW/cm^2 at the center of the laser spot. The power density of the 405 nm activation laser was adjusted to 15, 30, 60, 120, 240, and 480 W/cm^2 to evaluate the efficiency of photoactivation. Single-particle localization of the Pdots was performed using a custom MATLAB (MathWorks) script. The script used 5-10% of the intensity of the brightest pixel of all frames as a threshold to differentiate Pdots from background noise. The positions of Pdots were roughly located by searching for pixels above the threshold frame by frame and comparing their intensities to the adjacent pixel. The precise position of a Pdot was then determined by nonlinear least-squares fitting of a Gaussian function to the point spread function (PSF) of Pdots. Typically 7×7 pixels were used for the fitting (3 pixels on each side of the central pixel). The script then checked the FWHM obtained from the fitting to rule out the possibility of multiple adjacent Pdots or large aggregates.

Superresolution Imaging of MTs and CCPs

Superresolution imaging of MTs and CCPs was performed using the system described above. GLOX buffer was used for the spontaneous switching mode, while GLOX buffer containing 1% BME was used for the activation/deactivation mode. The excitation power typically used for imaging was 2-4 kW/cm^2 at the center of the laser spot. For the spontaneous switching mode, the activation laser was turned on at low power (5 W/cm^2) when there were not enough Pdots switched "on" per frame. For the activation/deactivation mode, periodic 405 nm laser pulses were used to randomly activate Pdots. The activation laser intensity was adjusted to ensure appropriate Pdot density. The autofocusing system was engaged to minimize axial focus drift. The experimental frame rate was adjusted to match the "on" duration of the Pdots, typically 5-50 Hz. 12000–24000 image frames were collected for reconstruction of superresolution images. The

images were analyzed using the ThunderSTORM plugin in imageJ as follows. Similar to the localization method described above, a threshold to search for Pdots was set to 3 times higher than the background noise fluctuation level. The pixels above the threshold were compared to 8 connecting neighbors to locate the approximate position of Pdots. For the activation/deactivation mode, frame by frame subtraction analysis was performed to reduce clustering artifact. The precise lateral position of a Pdot was determined by fitting the PSF to an elliptical Gaussian function. Typically 7×7 pixels were used for the fitting (3 pixels on each side of the central pixel). The FWHMs along the two axes were used to determine the axial position. For each kind of Pdot, the relationship between the aspect ratio of the PSF and the axial position was determined by imaging the corresponding undoped Pdots immobilized on a cover glass. We used a PIEZO stage (Thorlabs, APB302) to scan through multiple axial positions and monitored changes in PSFs throughout the process. The PSF width versus axial position data were fit to a polynomial function and imported to imageJ to be stored as a calibration standard.[4] To correct for lateral drift during the experiment, we employed the cross-correlation drift-correction method supplied by ThunderSTORM. Basically, the experimental image stacks were divided into small segments. For each segment, a superresolution image was constructed. Cross-correlation analysis was performed between the superresolution images of different segments to determine the lateral drift overtime. This method worked well as long as there were enough localized points for each segment. To perform two-color sequential imaging with Pdots, the sample was first excited by a 532 nm laser to image 10% PNDI-2F-doped CN-PPV Pdots, then excited by a 488 nm laser to image 10% PNDI-2F-doped CN-PDHFV Pdots. The emission filters used for 10% PNDI-2F-doped CN-PPV Pdots and 10% PNDI-2F-doped CN-PDHFV Pdots were 642/80 nm (Chroma, ET642/80m) and 525/50 nm (Chroma, ET525/50m), respectively. Image analysis was performed following the same procedures described above. Each individual single-color superresolution image was corrected for lateral drift according to the cross-correlation method described above. Since the interval between the two individual measurements was short, the two drifting functions obtained from the individual experiments were combined to calculate the lateral drift of the entire two-color experiment, which was used to generate the two-color overlay plot.

SUPPORTING RESULTS AND DISCUSSION

TEM Images of Pdots

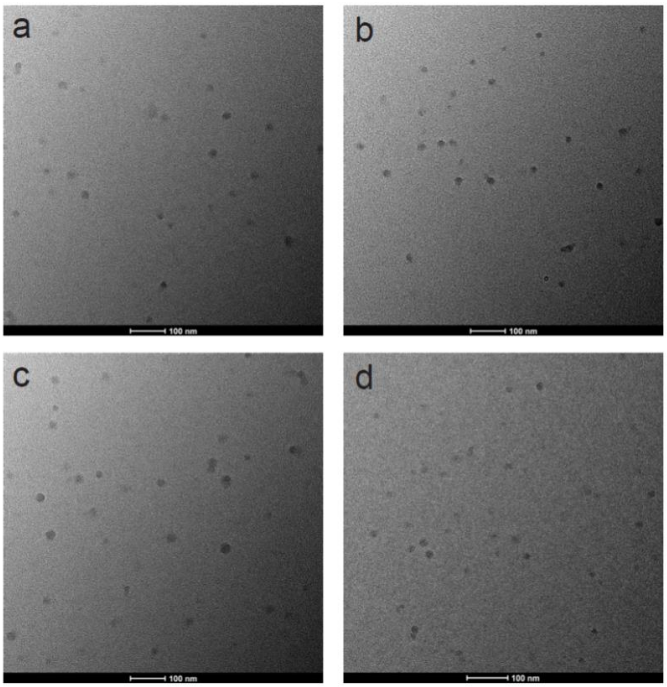

Figure S1. TEM images of (a) 10% PNDI-2F-doped CN-PDHFV Pdots, (b) 10% PNDI-2T-doped PFPV Pdots, (c) 20% PNDI-2F-doped F8BT Pdots, and (d) 10% PNDI-2F-doped CN-PPV Pdots.

Blinking Trajectory Analysis

Depending on the number of charge carriers recombined, the fluorescence intensity trajectories of the Pdots typically exhibited multiple "on" states. From the fluorescence intensity histogram, clusters of an "off" state and one or more "on' state(s) can be clearly observed (Figure S2). To differentiate "on" and "off" states, we set a threshold between the "off" state intensity peak and the first "on" state intensity peak and searched for events above the threshold. As discussed in the main text, when the Pdots were first exposed to excitation, the duty cycle decreased for a period of time until reaching a quasi-steady state. To determine the duty cycle induction time, we analyzed the single-particle fluorescence intensity trajectories with a sliding time window of 100 s and monitored changes in the "on" fraction over time. The "on" state durations and photon number per "on" event were determined after the duty cycle stabilized. To determine single-step "on" to "off" switching rate, only transitions between the "on" state 1 and the "off" state were considered. The obtained "on" state 1 duration histograms were fitted to a single exponential function to estimate charge generation/trapping rate in these Pdots (Figure S3). The single-step switching "off" rates determined from 10% PNDI-2F-doped CN-PDHFV Pdots, 10% PNDI-2T-doped PFPV Pdots, 20% PNDI-2F-doped F8BT Pdots, and 10% PNDI-2F-doped CN-PPV Pdots were 11 s^{-1}, 16 s^{-1}, 5 s^{-1}, and 9 s^{-1}, respectively (Figure S3).

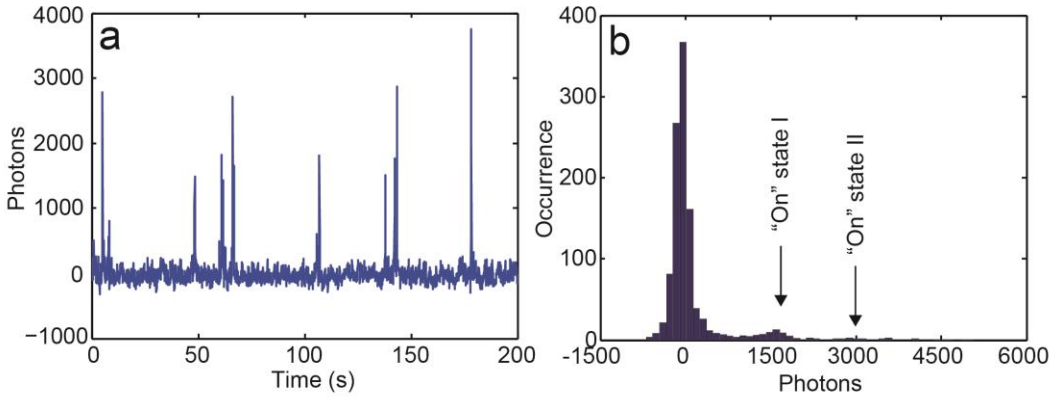

Figure S2. (a) Fluorescence intensity trajectory of a 10% PNDI-2F-doped CN-PPV Pdot. (b) Corresponding fluorescence intensity histogram, showing multiple "on" states.

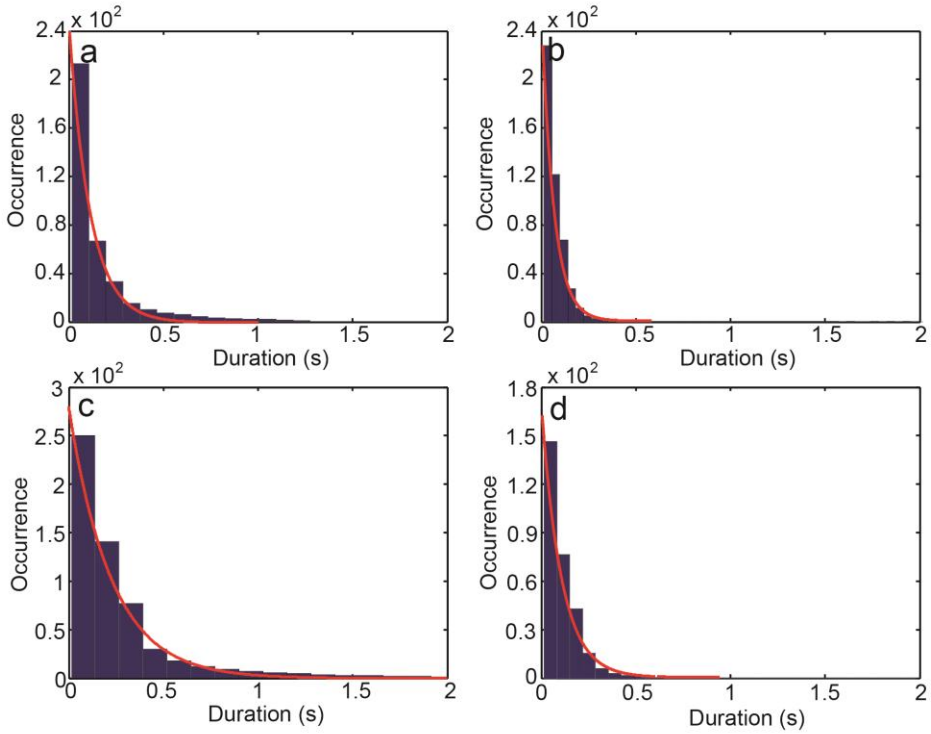

Figure S3. "On" duration histograms of (a) 10% PNDI-2F-doped CN-PDHFV Pdots, (b) 10% PNDI-2T-doped PFPV Pdots, (c) 20% PNDI-2F-doped F8BT Pdots, and (d) 10% PNDI-2F-doped CN-PPV Pdots, determined from single-step "on" to "off" transitions. The red lines represent single exponential fits to the distributions.

Representative Photoblinking Trajectories

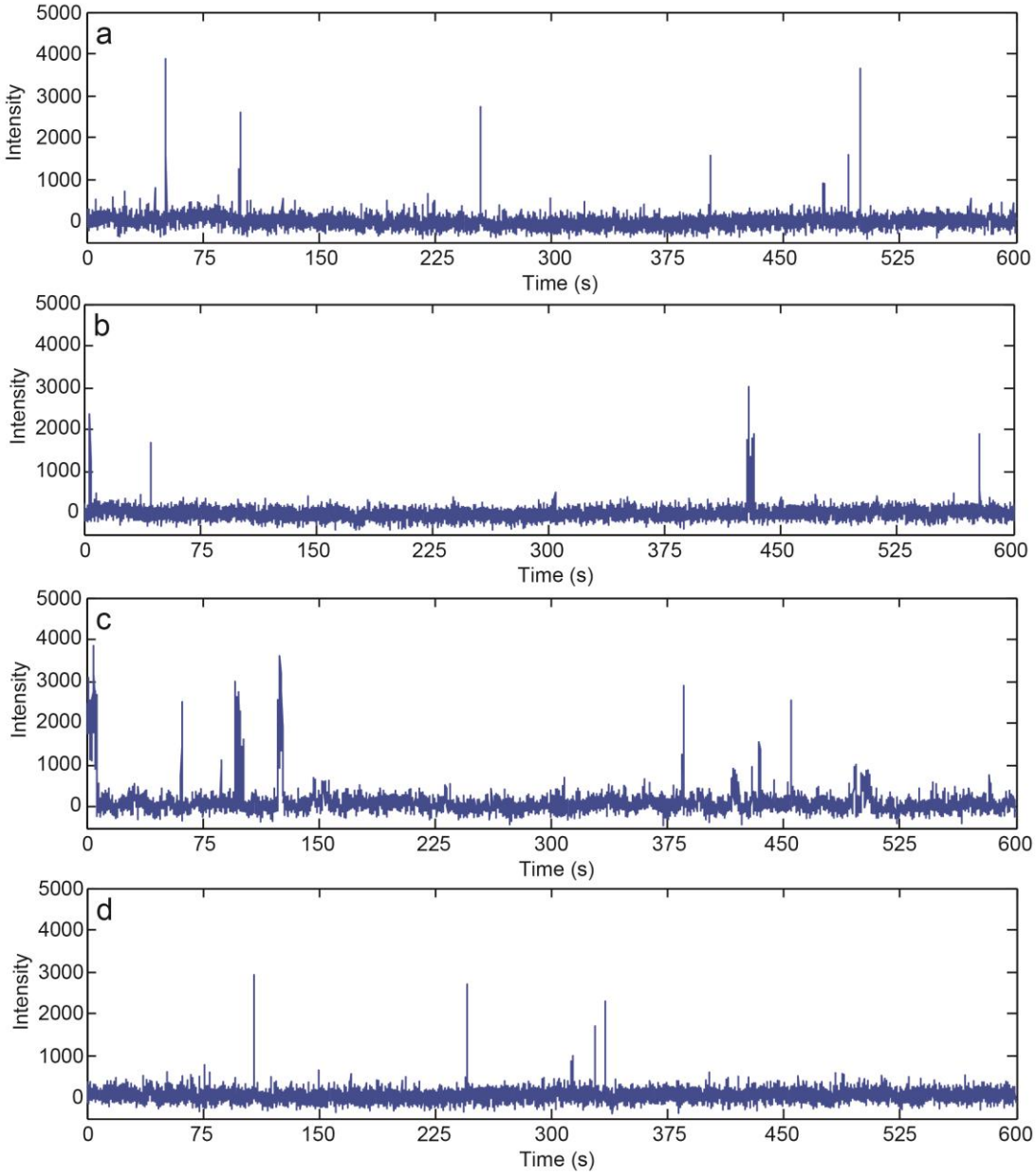

Figure S4. Representative photoblinking trajectories of (a) 10% PNDI-2F-doped CN-PDHFV Pdots, (b) 10% PNDI-2T-doped PFPV Pdots, (c) 20% PNDI-2F-doped F8BT Pdots, and (d) 10% PNDI-2F-doped CN-PPV Pdots, obtained at a 100 Hz frame rate, for determination of "on" state duration.

Simulation of Photoblinking and Photoactivation Dynamics

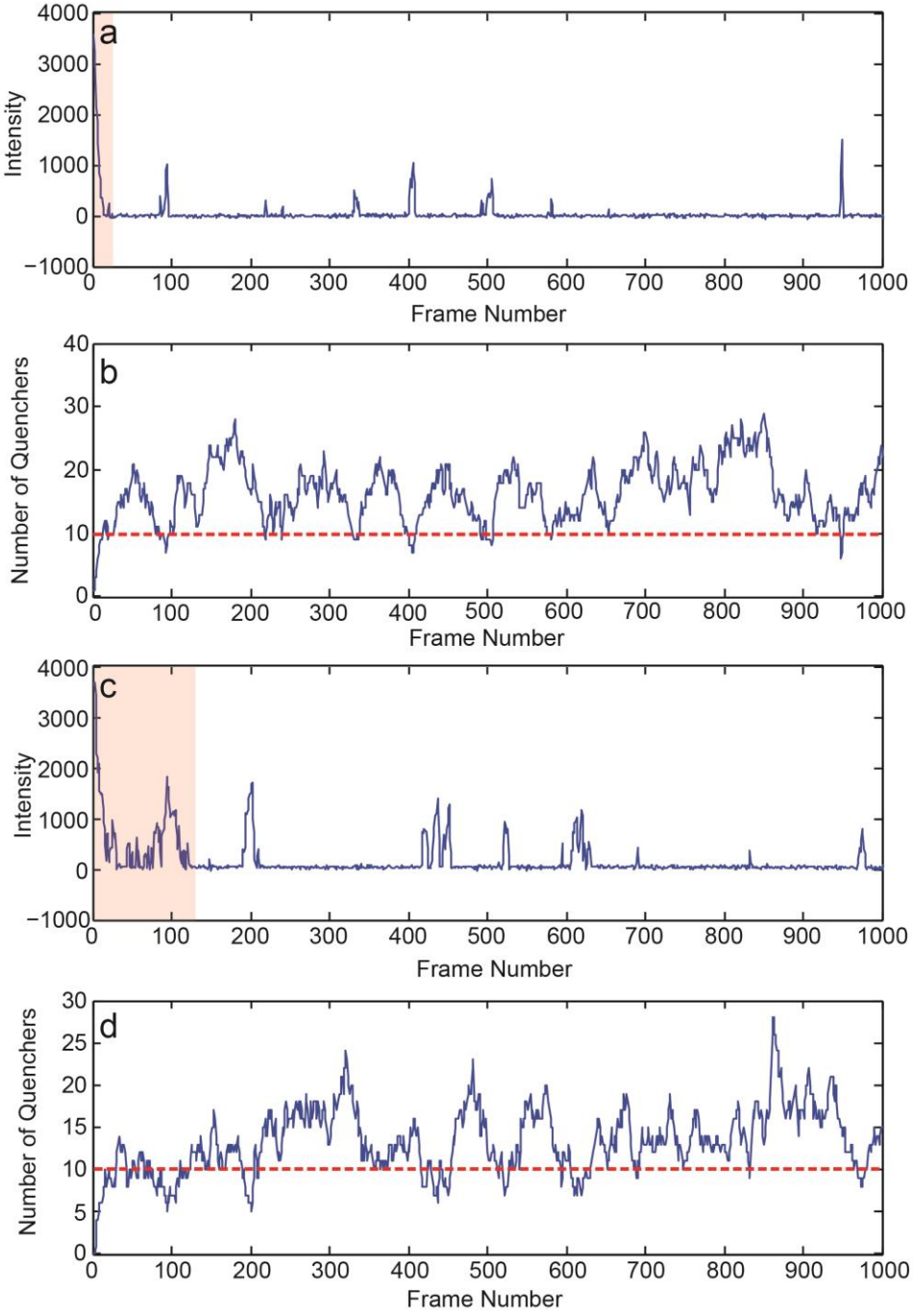

Figure S5 (a) Fluorescence intensity trajectory and (b) corresponding quencher population fluctuation trajectory, simulated using $k_{accum} = 9$ s^{-1}, $k_{recomb} = 0.5$ s^{-1}. Fluorescence intensity decay and duty cycle induction behavior is highlighted by the red band. (c) Fluorescence intensity trajectory and (d) corresponding quencher population fluctuation trajectory, simulated using $k_{accum} = 6$ s^{-1}, $k_{recomb} = 0.5$ s^{-1}. Fluorescence intensity decay and duty cycle induction behavior is highlighted by the red band

We used a kinetic model to qualitatively describe the photoblinking behavior observed, which is described as follows:

$$\frac{dn}{dt} = k_{accum} - k_{recomb}n, \quad (1)$$

where n is the number of charge carriers accumulated (trapped) in the light-emitting polymer phase. The charge accumulation rate depends on the (mobile) charge generation rate at the interface and the average energy barrier that a charge carrier needs to overcome to access these traps. We estimated k_{accum} from the single-step "on" to "off" switching rate, which was provided in the prior section. The second term on the right describes the recombination rate, which depends on the number of trapped charges and the average polaron lifetime in semiconducting polymers. Polaron lifetime reported by previous single molecule studies of similar semiconducting polymer systems typically ranged from 1–10 s. Polaron lifetime and k_{recomb} provide measurement of energetic discorder in Pdots. If we assume that detrapping is the rate-determining step in charge recombination and corresponds to a 1 nm energetic uphill hop, $k_{recomb} = 0.5$ s^{-1} yields an energy barrier of ~200 meV (calculated based on the Miller-Abrahams equation),[5] which is consistent with previously reported charge carrier trap depth in disordered polymer films.[6] We used $k_{accum} = 8$ s^{-1}, $k_{recomb} = 0.5$ s^{-1} to simulate the polaron population fluctuation trajectory shown in Figure 2k. The corresponding fluorescence trajectory shown in Figure 2j was simulated using the following equations,

$$I = I_0(1 - Q_e n), n < 10 \quad (2)$$

$$I = 0, n_p \geq 10 \quad (3)$$

where I_0 is the fluorescence intensity of Pdots without quencher and Q_e is the quenching efficiency of hole polarons. We assumed that each polaron has an equal quenching efficiency $Q_e = 10\%$ and that 10 polaron can completely quench the single-particle emission. It should be noted that there is likely variation in the quenching efficiency as it depends on local structure and the efficiency of energy funneling. However, such effects are difficult to model, and in any case should not change the fact that the hole polaron population fluctuations lead to "on" and "off" switching behavior, so we assumed the quenching efficiency of hole polaron to be uniform. According to the model, when the Pdots are first exposed to excitation, the hole polaron population grows from zero to a steady-state value, which leads to a rapid initial fluorescence intensity decay and duty cycle induction. The fluorescence decay and duty cycle induction time depend on polaron generation efficiency. As shown in Figure S5a, b, when $k_{accum} = 9$ s^{-1}, the fluorescence decay is fast and the duty cycle quickly approaches steady state. As k_{accum}

decreases to 6 s^{-1}, the fluorescence decay and duty cycle induction time become noticeably longer (Figure S5c, d). Less efficient polaron generation also leads to a smaller steady-state polaron population and more frequent "on" events. These phenomena are consistent with our experimental observations. To qualitatively visualize the photoactivation effect (Figure 2j, k), we increased k_{recomb} 3 times higher for 200 frames, starting from frame 8000. The equilibrium hole population quickly decreased from 16 to 5.3, which resulted in a much larger fraction of "on" time, similar to what we observed experimentally.

Survival Fraction Determination

The Pdots exhibited slow spontaneous thermal-assisted photoactivation, likely due to thermal-assisted detrapping and subsequent recombination of charge carriers. When the excitation light was blocked, the charge carrier population in the Pdots slowly decreased. As a result, when the Pdots were exposed to excitation again, a large fraction of Pdots were switched "on". The number of switched "on" particles per frame then gradually decreased for tens of seconds until the charge population in Pdots re-established equilibrium, as shown in Figure S6. The thermal activation behavior was used to determine the Pdot survival fraction. The initial number of Pdots immobilized on a coverslip was estimated by imaging at low power excitation before superresolution imaging. After 10 min of superresolution imaging, the Pdots were left in the dark for 30 min then imaged with both regular and 405 nm excitation to estimate the number of surviving Pdots.

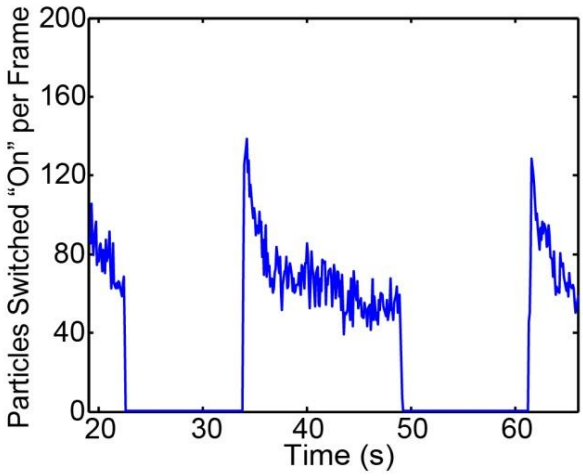

Figure S6. Number of switched "on" Pdots per frame, determined by imaging 10% PNDI-2F-doped CN-PDHFV Pdots immobilized on a glass coverslip.

Measurement of Axial and Lateral Localization Uncertainties

The lateral localization precision of a single particle is related to shot noise and the optical characteristics of the imaging system, and is given by [7]

$$\sigma = \sqrt{\frac{s^2}{N} + \frac{\alpha^2/12}{N} + \frac{8\pi s^4 b^2}{\alpha^2 N^2}}, \quad (4)$$

where s is the standard deviation (std) of the PSF, α is the pixel size, b is the background noise, and N is the detected photon number per frame. The std of the Pdots PSF is 130 nm. The pixel size of our setup is 110 nm. The background noise under the typical imaging condition is 5–20, which has contributions from readout noise, cell/background autofluorescence, and scattered light. For the Pdots in the photoswitching mode, the typical photon number per event ranges from 2800 to 6200. Based on these photon numbers and background noise of 20, the calculated theoretical localization uncertainties range from 6.0 to 3.0 nm. For the Pdots in the photoactivation/deactivation mode, the typical photon number per event ranges from 7800 to 16000. The calculated theoretical localization uncertainties range from 2.5 to 1.3 nm. The experimental localization uncertainty is expected to be higher due to additional errors introduced in drift correction as well as small focus drifts during the experiment.

The experimental localization uncertainties along different axes were obtained from imaging Pdots immobilized on a glass coverslip. The lateral position was determined from the fluorescence centroid, whereas the axial position was determined from the width of the PSF along the two axes. From each Pdot, we obtained a cluster of localized positions (Figure S7a). The localization uncertainties along different axes were determined from the standard deviations of the localization histograms obtained from dozens of Pdots (Figure S7b-d). The overall lateral localization precision was calculated as $(\sigma_x + \sigma_y)/2$. Typically, the axial localization uncertainty was ~2 times higher than the lateral localization uncertainty, consistent with previously reported results of the astigmatism method (table S1).[4] By analyzing localization clusters of Pdots non-specifically bound to cells at low density, we estimated that the in-cell localization precision of Pdots was close to the localization precision obtained on glass, with <10% difference.

Table S1. Experimental Localization Uncertainties of the Pdots

	10% PNDI-2F-doped CN-PDHFV Pdots	10% PNDI-2T-doped PFPV Pdots	20% PNDI-2F-doped F8BT Pdots	10% PNDI-2F-doped CN-PPV Pdots
Experimental lateral uncertainty in switching mode	10.2	12.9	7.8	13.5
Experimental axial uncertainty in switching mode	20.2	25.6	15.5	27.1
Experimental lateral uncertainty in activation mode	4.0	5.4	3.2	5.6
Experimental axial uncertainty in activation mode	8.0	10.7	6.3	11.2

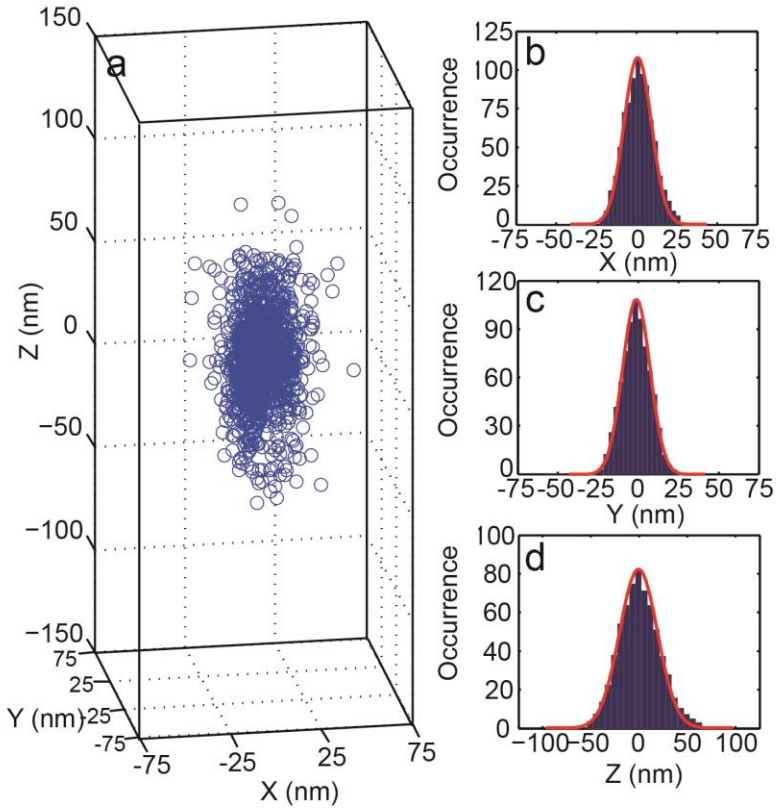

Figure S7. (a) 3D scatter plot of localized positions of a 10% PNDI-2F-doped CN-PDHFV Pdot immobilized on a glass coverslip. (b-d) Localization position histogram of 10% PNDI-2F-doped CN-PDHFV Pdots along the (b) X, (c) Y and (d) Z axis, fit to a Gaussian distribution with a standard deviation of 10.4, 10, and 20.2, respectively.

Repeated Activation and Deactivation Cycles of Pdots

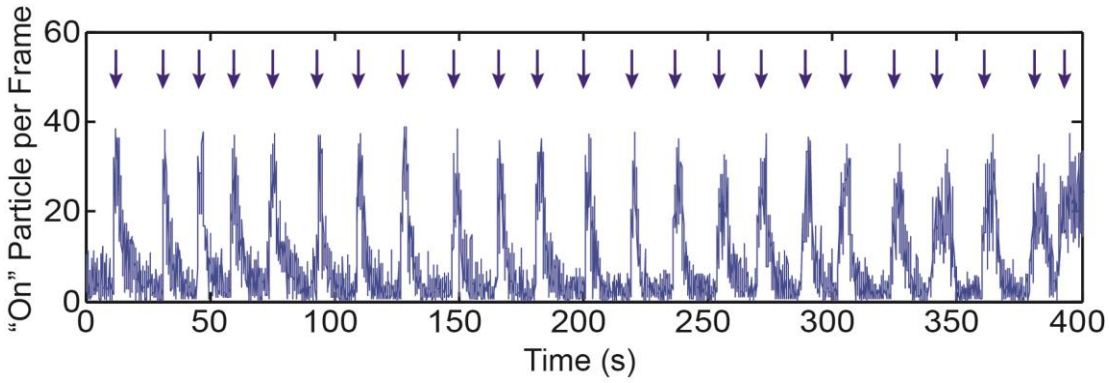

Figure S8. "On" particle per frame trajectory, showing repeated activation and deactivation cycles of 20% PNDI-2F-doped F8BT Pdots, for over 400 s. The activation laser pulses are indicated by the blue arrows.

Photon Number Histograms of the Two Imaging Modes

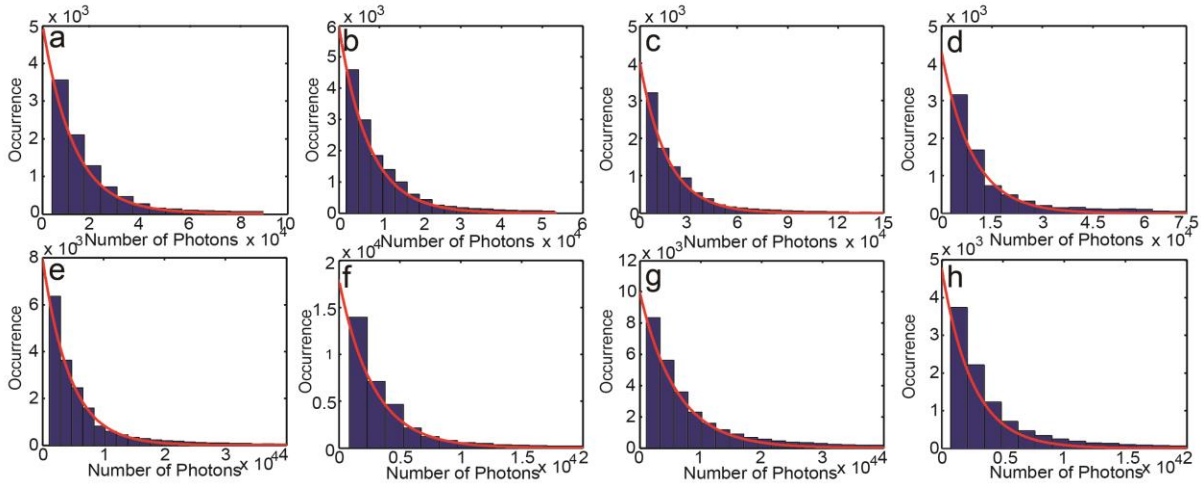

Figure S9. (a-d) "On" event photon number histograms of (a) 10% PNDI-2F-doped CN-PDHFV Pdots, (b) 10% PNDI-2T-doped PFPV Pdots, (c) 20% PNDI-2F-doped F8BT Pdots, and (d) 10% PNDI-2F-doped CN-PPV Pdots, obtained under photoactivation/deactivation mode. The red lines represent single exponential fits to the distributions. (e-h) "On" event photon number histograms of (e) 10% PNDI-2F-doped CN-PDHFV Pdots, (f) 10% PNDI-2T-doped PFPV Pdots, (g) 20% PNDI-2F-doped F8BT Pdots, and (h) 10% PNDI-2F-doped CN-PPV Pdots, obtained under spontaneous switching mode. The red lines represent single exponential fits to the distributions.

Superresolution Images of MTs and CCPs

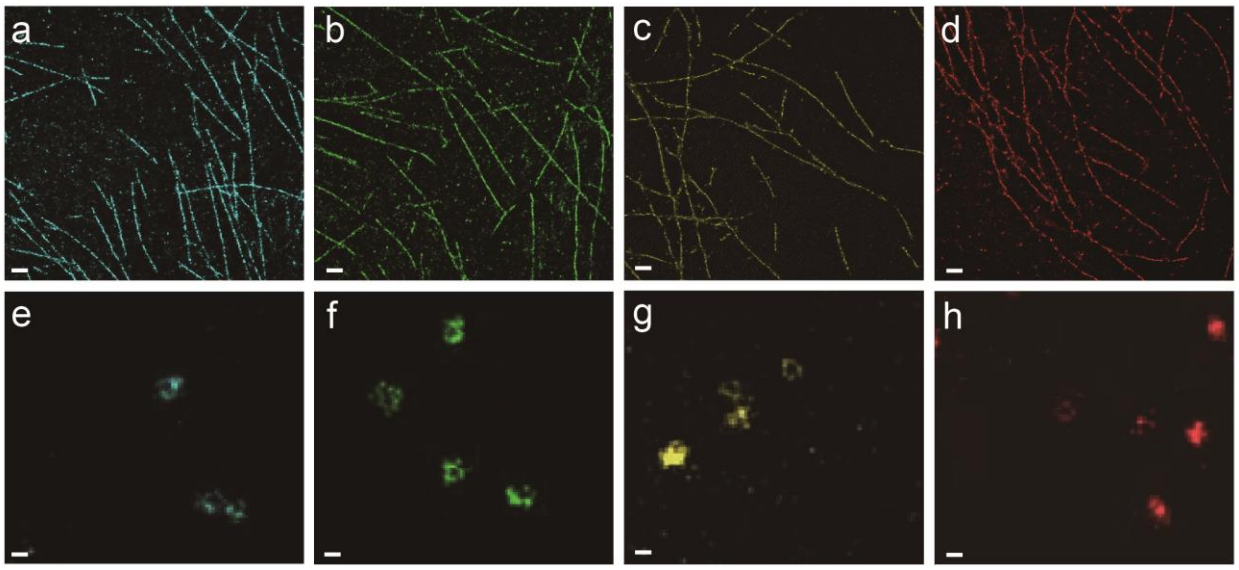

Figure S10. (a-d) Reconstructed superresolution images of MTs obtained using (a) 10% PNDI-2F-doped CN-PDHFV Pdots, (b) 10% PNDI-2T-doped PFPV Pdots, (c) 20% PNDI-2F-doped F8BT Pdots, and (d) 10% PNDI-2F-doped CN-PPV Pdots, under photoactivation/deactivation mode (scale bars, 1 μm). (e-h) Reconstructed superresolution images of CCPs obtained using (e) 10% PNDI-2F-doped CN-PDHFV Pdots, (f) 10% PNDI-2T-doped PFPV Pdots, (g) 20% PNDI-2F-doped F8BT Pdots, and (h) 10% PNDI-2F-doped CN-PPV Pdots, under spontaneous switching mode (scale bars, 100 nm).

Calibration Curve for 3D Astigmatism Microscopy

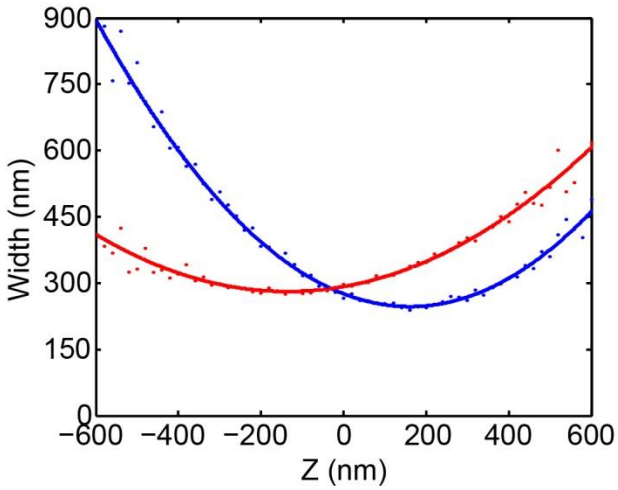

Figure S11. Calibration curve of PSF widths along X (blue) and Y (red) axes, at different axial positions, obtained from imaging undoped F8BT Pdots immobilized on a glass coverslip. Each data point represents the average value of 25 Pdots.

Labeling Density of Pdots and Dye Conjugated Antibodies

Here, we used MTs as a model system to compare the labeling density of dye conjugated primary antibodies and Pdots. MTs can be considered as 25 nm diameter cylinders consisting of two alternating proteins: α- and β-tubulin. Immunoglobulin G (IgG) antibodies have two arms that bind to antigens (α-tubulin) and one leg that conjugates to dyes or biotins. The overall dimension is 14.5×8.5×4 nm.[8] Pdots are ~15 nm in diameter. The cross-section of an immunostained MT was plotted in Figure S12, which was adapted from the previous publication.[9] Specifically, the MT is a cylinder with repeated threads of proteins. Antibodies and Pdots were plotted in two different shades to represent labeling of two adjacent threads. The size of IgG was adjusted to account for rotation effect. As shown in the plot, dye conjugated antibodies and streptavidin conjugated Pdots exhibit an equal labeling density with all α-tubulin labeled. Pdots did not reduce labeling density as they exhibit a comparable size as the IgG binding arms and are located at the outer layer of the immunostained MTs. The major difference between dye conjugated antibody and Pdot labeling is that Pdots are located further away from the MTs as compared to dyes. As shown in Figure 4h, the two peaks in the MT cross-section plot are separated by 45 nm, while for dye conjugated antibody labeled MTs, this value is typically 34-36 nm.[10] In both cases, the MT sizes are overestimated, which is a common artifact in superresolution imaging. The broadening artifact caused by IgGs has been previously studied. Typically, a single layer of IgGs can increase MT diameter by 8-10 nm, depending on the orientation of IgGs.[9] After taking the sizes of IgGs and 10% PNDI-2F-doped CN-PDHFV Pdots (14 nm) into account, we obtained a MT diameter of 21-23 nm, which is in good agreement with previously reported MT diameter of 25 nm. The small underestimation is possibly caused by the fact that we used hydrodynamic radius (distance from particle center to slipping plane)

determined by DLS to perform the correction. Overall, our model suggests that, when IgG antibodies are used for labeling, Pdots do not result in significantly lower labeling density as compared to dyes. Experimentally, using a structure that both Pdots and dyes are capable of resolving (CCPs), we compared the labeling density of the two and observed no obvious difference (Figure S13). In the rare situation that requires extremely high labeling density, nanobodies are typically used instead of IgG antibodies. In such case, Pdot size can be conveniently reduced using the cross-flow filtration method that we previously reported to suit the need of the application.[11]

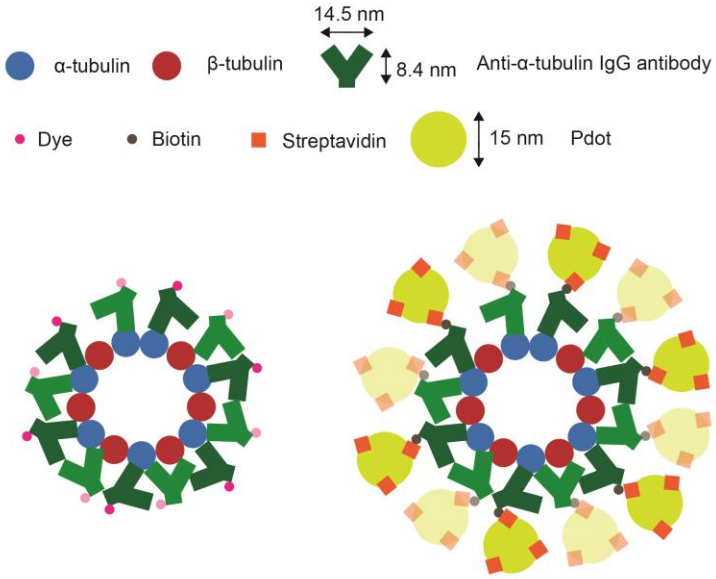

Figure S12. Cross-section plots of MTs labeled with dye-conjugated IgG antibodies (left) and IgG antibodies/Pdots (right). Since MT is a cylinder with repeated threads of proteins, we plotted antibodies and Pdots in two different shades to visualize the labeling of two adjacent threads.

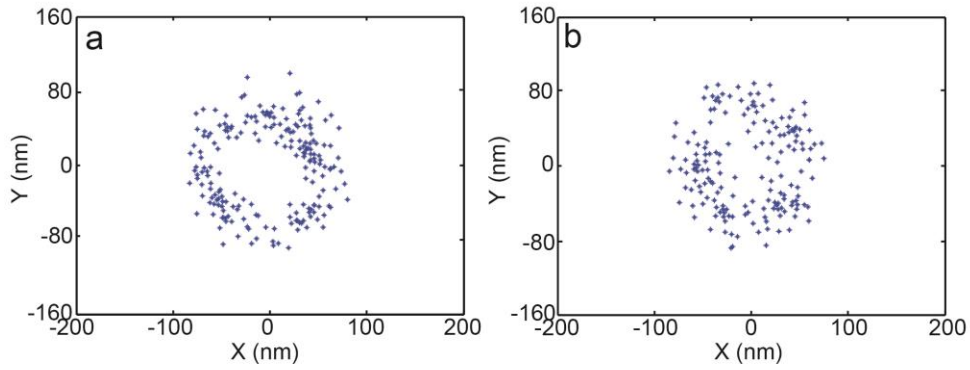

Figure S13. Localization scatter plot of CCPs labeled with IgG antibodies/10% PDNI-2F-doped CN-PDHFV Pdots (a) and Alexa 647-conjugated IgG antibodies (b), showing no obvious difference in labeling density.

MT Structures Resolved by Confocal and Superresolution Imaging

Here, we compared the resolution of the spontaneous switching superresolution imaging and confocal (diffraction limited) imaging. A confocal image of Pdots label MTs is given in Figure S14a, showing unresolved clusters of MTs. In figure S14b, c, diffraction limited and superresolution images of MTs acquired in the same region of interests were directly compared, showing that superresolution imaging is capable of resolving densely pack MTs that cannot be resolved using diffraction limited imaging techniques.

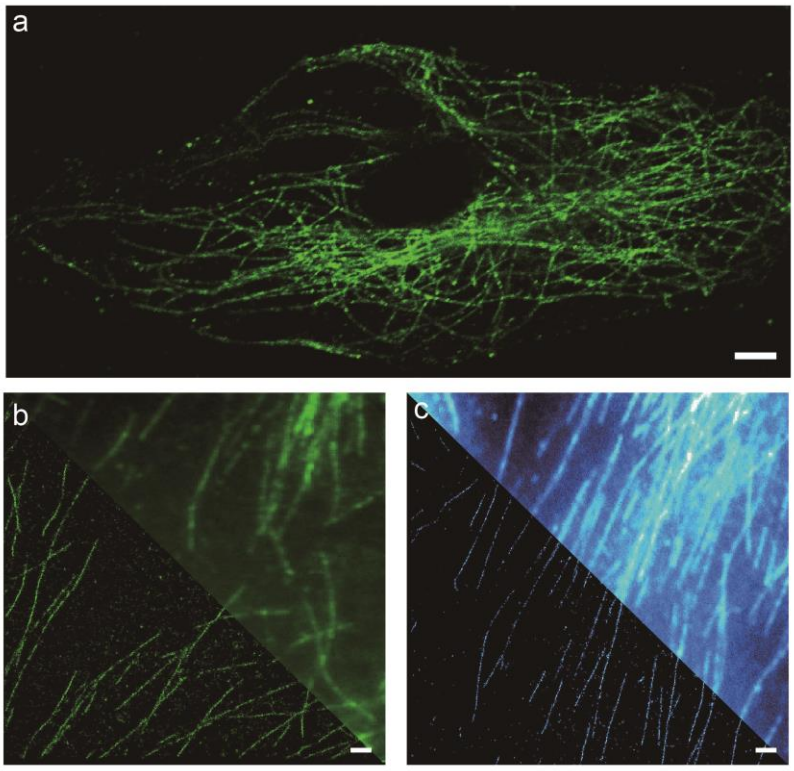

Figure S14 (a) A confocal image of MTs labeled with F8BT Pdots, scale bar 5 μm. (b, c) Comparison of spontaneous switching mode superresolution and diffraction limited images of MTs, labeled with 10% PNDI-2F-doped PFPV (b) and 20% PDNI-2F-doped F8BT Pdots (c), scale bar 1 μm.

REFERENCES

[1] C. Wu, C. Szymanski, J. McNeill, *Langmuir* **2006**, *22*, 2956-2960.

[2] C. Wu, T. Schneider, M. Zeigler, J. Yu, P. G. Schiro, D. R. Burnham, J. D. McNeill, D. T. Chiu, *J. Am. Chem. Soc.* **2010**, *132*, 15410-15417.

[3] A. R. Halpern, M. D. Howard, J. C. Vaughan, *Curr. Prot. Chem. Biol.* **2015**, *7*, 103-120.

[4] B. Huang, W. Wang, M. Bates, X. Zhuang, *Science* **2008**, *319*, 810-813.

[5] a) H. Bässler, *Phys. Status Solidi B* **1993**, *175*, 15-56; b) N. Tessler, Y. Preezant, N. Rappaport, Y. Roichman, *Adv. Mater.* **2009**, *21*, 2741-2761.

[6] R. Noriega, J. Rivnay, K. Vandewal, F. P. Koch, N. Stingelin, P. Smith, M. F. Toney, A. Salleo, *Nat. Mater.* **2013**, *12*, 1038-1044.

[7] R. E. Thompson, D. R. Larson, W. W. Webb, *Biophys. J.* **2002**, *82*, 2775-2783.
[8] Y. H. Tan, M. Liu, B. Nolting, J. G. Go, J. Gervay-Hague, G.Y. Liu, *ACS Nano* **2008**, *2*, 2374-2384.
[9] J.-B. Chang, F. Chen, Y.-G. Yoon, E. E. Jung, H. Babcock, J. S. Kang, S. Asano, H.-J. Suk, N. Pak, P. W. Tillberg, A. T. Wassie, D. Cai, E. S. Boyden, *Nat. Methods* **2017**, *14*, 593.
[10] G. T. Dempsey, J. C. Vaughan, K. H. Chen, M. Bates, X. Zhuang, *Nat. Methods* **2011**, *8*, 1027-1036.
[11] Y. Jiang, J. McNeill, *Nat. Commun.* **2018**, *9*, 4314.